applied optics

Stent optical inspection system calibration and performance

Carlos Bermudez,[1,2,*] Ferran Laguarta,[1] Cristina Cadevall,[1,2] Aitor Matilla,[2] Sergi Ibañez,[3] and Roger Artigas[1,2]

[1]Center for Sensors, Instruments and Systems Development (CD6), Technical University of Catalonia (UPC), Rambla Sant Nebridi 10, E-08222 Terrassa, Spain
[2]Sensofar-Tech, S.L., Parc Audiovisual de Catalunya, Ctra. BV1274 km 1, E-08225 Terrassa, Spain
[3]Sensofar-Medical, S.L., Parc Audiovisual de Catalunya, Ctra. BV1274 km 1, E-08225 Terrassa, Spain
*Corresponding author: bermudez@sensofar.com

Received 14 October 2016; revised 11 January 2017; accepted 11 February 2017; posted 13 February 2017 (Doc. ID 278329); published 9 March 2017

Implantable medical devices, such as stents, have to be inspected 100% so no defective ones are implanted into a human body. In this paper, a novel optical stent inspection system is presented. By the combination of a high numerical aperture microscope, a triple illumination system, a rotational stage, and a CMOS camera, unrolled sections of the outer and inner surfaces of the stent are obtained with high resolution at high speed with a line-scan approach. In this paper, a comparison between the conventional microscope image formation and this new approach is shown. A calibration process and the investigation of the error sources that lead to inaccuracies of the critical dimension measurements are presented.

OCIS codes: (110.0180) Microscopy; (120.3930) Metrological instrumentation; (120.3940) Metrology; (120.4630) Optical inspection.

https://doi.org/10.1364/AO.56.00D134

1. INTRODUCTION

In recent times, stent manufacturing has grown exponentially. Stents are miniature hollow cylinders that are implanted into the human body to remove a stenotic lesion or to facilitate access for surgery. They are manufactured from raw tubes, which are laser-cut. Some of the most important processes during the manufacturing of a stent are dimensional control and visual inspection. Defects and shape deviations from the nominal design affecti its performance, lifetime, and even cause a hazard to the patient. Stent quality assurance processes are tremendously strict. Inspection of a stent is today an extremely labor-intensive, time-consuming, and expensive process, executed visually by skilled operators equipped with optical microscopes. Human errors can eventually yield samples out of specifications, and increase stent rejection, which ends with higher manufacturing costs.

Few automated inspection systems (using contact and noncontact techniques) have been proposed in recent years to provide objectivity, repeatability, and speed to the inspection process. One of the first developments is based on a stent inserted onto a mandrel, which is rotating, illuminated with a backlight, and imaged with a line-scan camera [1]. Another approach to avoid some of the limitations of the mandrel is the use of two rollers with dual illumination [2]. However, those systems use telecentric optics to form the image of the surface of the stent, using low numerical aperture, and thus recover images with low resolution [3]. Another disadvantage is that they do not measure the inner surface of the stent.

In this paper, an optical, high-resolution inspection system is presented. Our approach uses a high numerical aperture imaging optics, a triple-light illumination arrangement (epi-illumination, back and side), a CMOS camera, and a high-precision rotational stage aimed to obtain unrolled images of all stent surfaces [4]. We provide well-focused and high-contrast images of the outer, inner, and side surfaces with up to 1 μm lateral resolution. The obtained images are used for measuring strut dimensions, roundness quality of the edges after the polishing stage, and also for detection and classification of defects.

2. EXPERIMENTAL SETUP

To perform accurate stent dimensional metrology, it is essential to acquire well-focused and high-contrast images. To acquire such images we have implemented the following approach: a microscope arrangement with the use of high numerical aperture optics, a triple illumination system, a CMOS camera that can behave as both area and line scan, and a high-precision rotational stage. In a bright-field microscope, the image of stent-like samples decreases in light gathering and focus for those regions far from the apex [Figs. 1(a) and 1(c)]. With the line scan mode

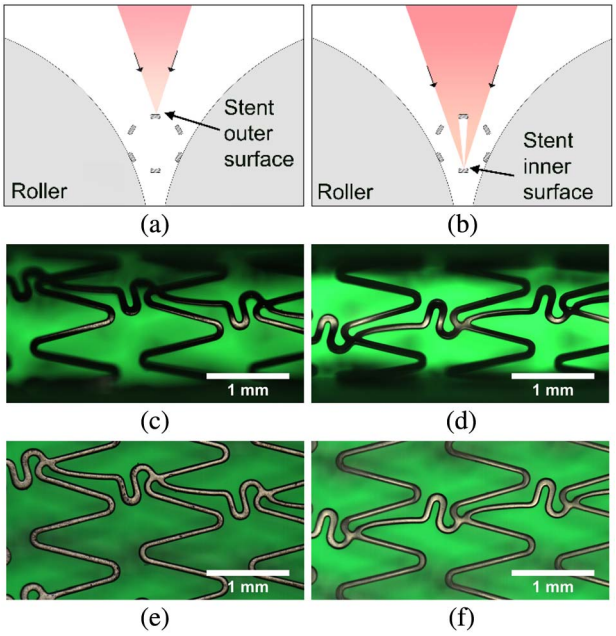

Fig. 1. Schematic of a stent cross section, focusing the (a) outer and (b) inner surfaces. Images taken with a 5× 0.15 NA. Outer surface: (c) bright-field screenshot, and (e) part of a line-scan acquired section. Inner surface: (d) bright-field screenshot, and (f) part of a line-scan acquired section.

of the camera and the rotational stage rotating at a continuous speed, we compose the image, acquiring data from the apex of the stent [Fig. 1(e)]. A similar process is used for the inner surface. Light rays can cross the outer or upper surface since its struts cover only a relatively small part of the field of view (FOV) [Fig. 1(b)], and they appear defocused. This allows focus of the inner surface with high contrast [Fig. 1(d)], and it is imaged using the same line-scan approach [Fig. 1(f)].

Figure 2 shows the optical and mechanical arrangement of our approach. A white-light LED illuminates the field diaphragm of a microscope and is imaged onto the entrance pupil of a microscope objective in a Köhler-type illumination scheme. The light reflected from the stent surface is going back to the objective, which is forming an image onto an area scan camera. Two additional light sources are located at one side and under the roller stage to provide diffuse back and side illumination, the latter intended to facilitate visual inspection for the user and for further investigation related to stent sidewall imaging. The resulting image can be seen in Fig. 1(a). With the use of a motorized nosepiece, we used microscope objective magnifications ranging from 2.5× to 20× with numerical apertures from 0.075 to 0.45. This provides the possibility to acquire images with a very large FOV (2.5×: 7.20 mm horizontal, 3.52 μm lateral resolution) or keeping an optical resolution below 1 μm (20×: 0.9 mm horizontal FOV, 0.44 μm lateral resolution).

The camera used in this study is capable of acquiring in area scan mode (2 million pixels) or line scan (2048 pixels) at much higher frequency. Unrolled images as shown in Fig. 1(b) are obtained with the line scan mode of the camera and with the rotational stage rotating at continuous speed. The rotational

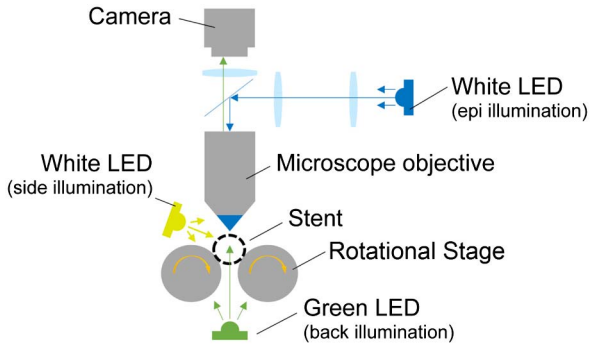

Fig. 2. Triple illumination system arrangement.

stage is a two-roller arrangement consisting of two stainless steel nuclei rollers enclosed with a white polyoxymethylene (POM) 2 mm thick cover to provide enough stiffness and a smooth surface (Ra < 0.8 μm). Light reflections are avoided thanks to the elevated diffusion capacity of the plastic. Roller diameter and distance between them is optimized to maintain enough back light aperture while providing the possibility to focus short working distance objectives, such as a 20× 0.45 NA with a working distance of 4.5 mm, and at the same time able to focus in the inner surface of stents ranging from 1.5 to 15 mm in outer diameter (OD) without being limited by the rollers.

3. CRITICAL DIMENSIONS

The most common dimensional analyses in stent inspection are strut width and edge roundness. We use segmentation algorithms to isolate stent struts from the background. We obtain binary masks from strut outer geometry of Fig. 3(a) and edge geometry with the use of morphological operations and a blob detection algorithm [Figs. 3(b) and 3(c)]. From the original image and said binary masks, critical dimension analysis, defect detection and classification, and further 3D metrology investigation can be performed.

A. Critical Dimensions Measurement

We have analyzed the differences when measuring critical dimensions with a conventional microscope in comparison to our unrolled images. Conventional microscope images measure the projected surface width, while unrolled images measure the arc section of the strut. The result is a larger measurement, which fits exactly to the nominal design, but not to what the inspection operators are used to measure. In Fig. 4, a stent section is shown. Strut width *CD* can be defined as a function of

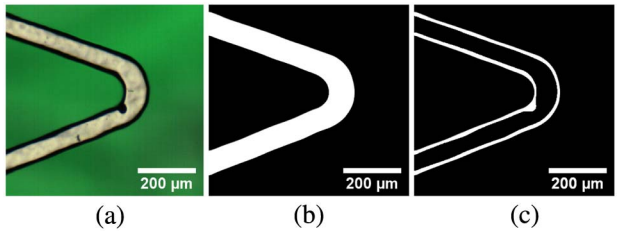

Fig. 3. Stent with a crack defect: (a) unrolled image, (b) surface mask, and (c) edge mask.

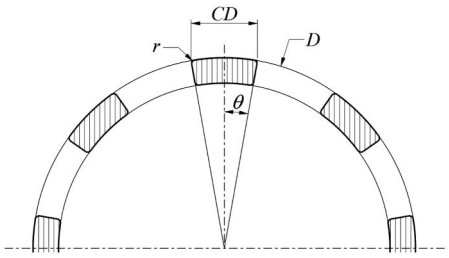

Fig. 4. Section of a stent strut.

the stent outer diameter D, the roundness radius r of the edge, and the angle formed by its walls with the observation axis, θ.

Assuming the strut does not have rounded edges, that is, without surface treatment, its critical dimension in a conventional microscope may be described as

$$CD_M = 2\left(\frac{D}{2}\sin(\theta)\right). \tag{1}$$

The factor of 2 takes into account that θ corresponds to one-half of the strut, while in an unrolled image the critical dimension corresponds to 2 times the arc length:

$$CD_U = 2\left(\frac{D}{2}\theta\right). \tag{2}$$

Surface treatment has an effect on critical dimension measurements due to the modification of the stent edge geometry. Figure 5 shows the difference between a non-treated, sharp-edge strut [Fig. 5(a)] versus its geometry after surface treatment [Fig. 5(b)], CD'_M being the critical dimension measured with the microscope with rounded edges.

This critical dimension CD'_M is determined by

$$CD'_M = 2\left(\sin(\theta)\sqrt{\frac{D^2}{4} - Dr} + r(1-\cos(\theta))\right)\Big|_{\theta>\theta_{\mathrm{MIN}}}, \tag{3}$$

where r is the radius of the edge roundness. This expression is valid only for a certain interval, $\theta > \theta_{\mathrm{MIN}}$, which stands for the limit where roundness diameter equals strut thickness, meaning that smaller struts have no sense. Figure 6 shows the relationship of this limitation between stent diameter and edge roundness radius.

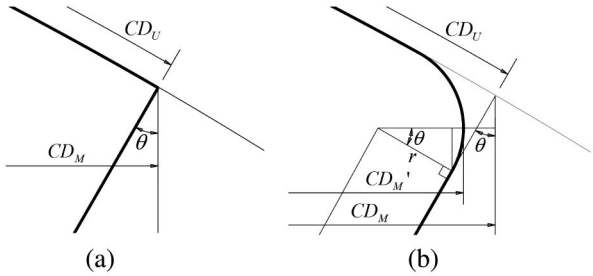

Fig. 5. Zoom view of a strut edge (a) without surface treatment and (b) with surface treatment.

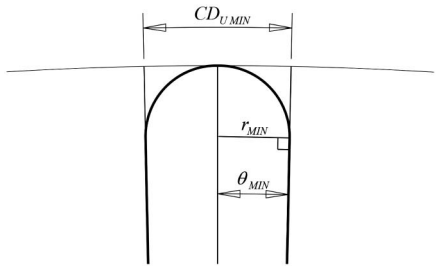

Fig. 6. Minimum strut width is determined by the roundness radius.

The minimum angle θ_{MIN} can be obtained through

$$\theta_{\mathrm{MIN}} > \arcsin\left(\frac{r_{\mathrm{MIN}}}{D/2 - r_{\mathrm{MIN}}}\right). \tag{4}$$

By substituting Eq. (4) into Eq. (2), the minimum strut width $CD_{U\,\mathrm{min}}$ is defined as

$$CD_{U\,\mathrm{MIN}} > D\arcsin\left(\frac{r}{D/2 - r}\right). \tag{5}$$

Therefore, by substituting Eq. (3) into Eq. (2) and taking into account the condition in Eq. (5), we obtain that the critical dimension of a stent with rounded edges measured with a microscope is the following:

$$CD'_M = 2\left(\sin\left(\frac{CD_U}{D}\right)\sqrt{\frac{D^2}{4} - Dr} + r\left(1-\cos\left(\frac{CD_U}{D}\right)\right)\right)\Big|_{CD_U>CD_{U\,\mathrm{MIN}}}. \tag{6}$$

We can assert that the ratio between a measurement in a conventional microscope versus one in an unrolled image is dependent on edge roundness, and the difference between them is increasing together with the strut width. Figure 7 shows the ratio between CD'_M and CD_U versus the strut width CD_U for a stent with outer diameter of 1.5 mm and with different edge roundness.

We have checked this behavior with an electropolished 1.5 mm diameter stent with 30 μm roundness radius. Two profile cuts have been obtained at the same stent location (Fig. 8), and the measurement of such profiles shows a strut width of

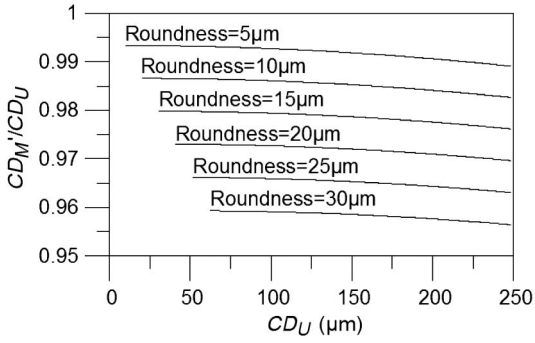

Fig. 7. Critical dimension measurement ratio between a conventional microscope image and an unrolled acquisition, for six given strut edge roundness values of a 1.5 mm outer diameter stent.

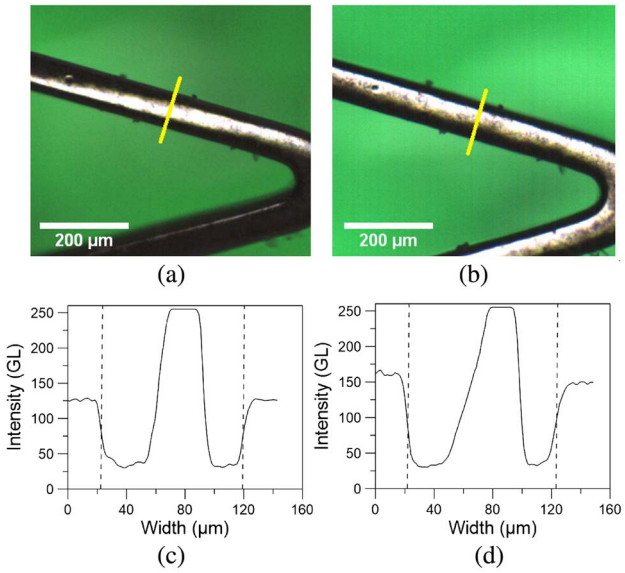

Fig. 8. Critical dimension measurement comparison between (a) a conventional microscope screenshot and (b) an unrolled acquisition. Width results are (c) 97.1 µm for the screenshot profile and (d) 101 µm for the unrolled acquisition profile.

97.1 µm in the screenshot (conventional microscope image) versus 101.0 µm corresponding to the unrolled image, revealing a measurement ratio CD'_M/CD_U of 0.96. Strut width measurement is done by automatically locating maxima of the first derivative of the profile cut intensity [vertical dashed lines in Figs. 8(c) and 8(d)].

4. CALIBRATION

Critical dimension measurement accuracy is achieved through a calibration process of the complete setup. This process consists of precise alignment of the roller stage with the optical axis, calibration of the optical system magnification and rotational speed, adjusting the parfocal and parcentric objective offsets, and fine-tuning the camera acquisition time to avoid aliasing with the illumination frequency switching. Because there is no commercially available specimen for magnification calibration in the unrolled direction, we have manufactured ourselves a state-of-the-art calibration specimen for unrolled image acquisition.

A. Roller Stage and Stent Position

To ensure the proper focusing of the microscope objective onto the surface, the geometry and positioning of the rollers with respect to the optical axis must be calibrated.

It is important to note that this calibration procedure has to be performed with one single objective, in our case a 5× magnification objective, because different parfocality and parcentricity errors appear between objectives, as will be seen in Section 4.C.

The first step is to know exactly the central position between the two rollers in the Y direction (transversal to the stent), where the stent will be placed. The X position (longitudinal to the stent axis) is irrelevant in this step. This is done by acquiring one image around the central region where the back illumination should be

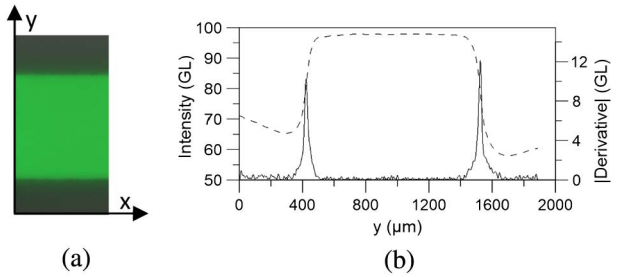

Fig. 9. (a) Back side illumination enabled, focusing the rollers edges and (b) filtered mean profile (dashed line) and its derivative (modulus, solid line).

centered. Although rollers are out of focus [Fig. 9(a)], the sum of all the image columns [dashed line in Fig. 9(b)] allows detecting the center between them. In our case we apply a Savitzky–Golay derivative with a nine-point window size to detect the edge transition [solid line in Fig. 9(b)].

Once the derivative of the average intensity profile is obtained, a peak detection algorithm is applied around the peaks with a parabolic fitting. This provides subpixel accuracy, meaning less than 1 µm positioning resolution. If the result value is not aligned with the optical axis, the corresponding offset to the Y stage is automatically applied. The algorithm runs again to compensate a slight deviation that may be remaining due to the effect of back light projection and numerical aperture.

The next calibration step is to find the rollers' Z height. First, the Y stage is moved a distance corresponding to half the separation between the two rollers' axes, in our case 5.95 mm, and the Z stage to the height where the apex of the roller is located. This value is known by design.

At this point, an autofocus algorithm is carried out, which finds the highest contrast plane using an image processing algorithm that looks for the image variance, taking advance of the roller surface irregularities.

Afterward, the Y stage is moved to the second roller apex to find its height with the same procedure. The average of the two apex heights determines the rollers' average height at the optical axis. If the two heights are different, a skewness error appears. This skewness makes the Z value found valid only for a range of stent diameters whose apex is near one of the rollers, as it will be seen in the next section.

Once the Y stage is aligned with the optical axis and the Z position of the rollers' apex is known, the position of any stent outer diameter can be obtained by simple geometrical calculations, as can be observed in Fig. 10.

Finally, the height of the stent apex Z is determined by

$$Z = h_{AF} - \frac{D_R}{2} + \sqrt{\left(\frac{D_R}{2} + \frac{D}{2}\right)^2 - \frac{S^2}{4}} + \frac{D}{2}, \tag{7}$$

where D_R stands for roller diameter, S is the separation between the two roller axes, D is the stent diameter, and h_{AF} the height of the rollers' apex determined by the autofocus algorithm.

B. Optical Magnification

The real optical magnification of the microscope objective is calibrated with a magnification calibration specimen for

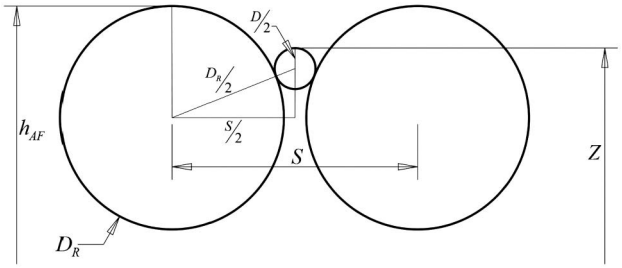

Fig. 10. Determination of outer diameter Z position.

microscopes in the X direction. The unrolled direction magnification is dependent on the acquisition frame rate and the rotational speed. We developed a custom calibration specimen to calibrate the rotational speed at a given, fixed frame rate. The specimen consists of a chromium-coated rod lens and laser-engraved Ronchi grating parallel to the radial direction, with 50 μm pitch.

1. X Magnification

The microscope's real optical magnification is calibrated by a certified calibration specimen, in our case, a 150 mm long ruler with 10 μm Ted Pella model MR1 [Fig. 11(a)]. With the microscope objective, a 125 mm tube lens, and a camera with 5.5 μm pixel size, we obtain a sampling as is depicted in Table 1.

To calibrate the magnification, an algorithm extracts the intensity profile of the optical ruler around the marks [Fig. 11(b)] and calculates the mean distance between them through the PS_m parameter (ISO 4287), which determines the average value of the element spacing.

Once the average width between the ruler marks is obtained, it is divided by the nominal value (10.0 μm) to obtain the calibration factor. This procedure is repeated for every objective.

2. Rotation Speed

Although the real optical magnification for a bright-field image can be calibrated with an optical ruler, the magnification in the Y direction of an unrolled image is given by two additional parameters: the camera frame rate and the rotating speed. The acquisition frame rate has to be fixed to a certain value

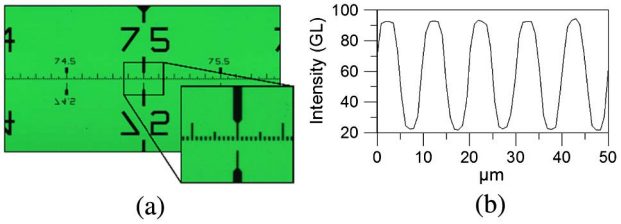

Fig. 11. (a) 150 mm, 10.0 μm resolution optical ruler and (b) intensity profile at the center of the ruler.

Table 1. Optical Sampling for Different Magnifications

Magnification	2.5×	5×	10×	20×	50×
Sampling (μm)	3.52	1.76	0.88	0.44	0.176

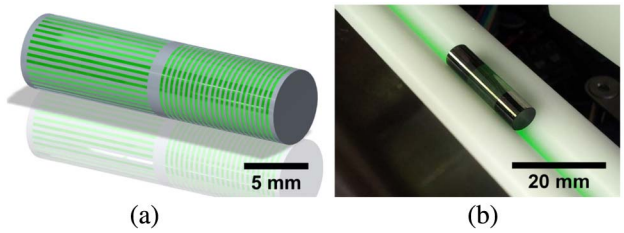

Fig. 12. (a) 3D representation of the calibration specimen and (b) picture of the calibration rod, 5 mm ∅ × 20 mm.

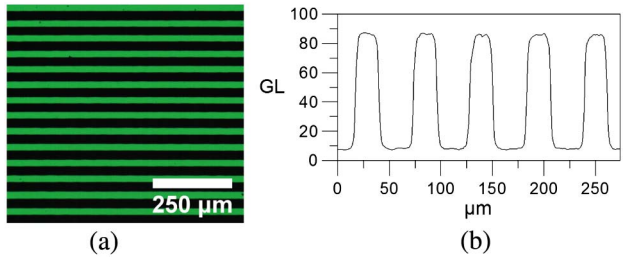

Fig. 13. (a) Unrolled image of the calibration specimen and (b) average vertical light intensity profile.

in order not to cause aliasing with the illumination board switching frequency, as it will be seen in Section 4.D. Therefore, the variable parameter is the rotating speed, which is also dependent on the magnification.

In our case, we have manufactured our own custom calibration specimen on a cylindrical lens of 5 mm × 20 mm, coated with a 300 nm chromium film and laser engraved with a 50 μm Ronchi grating. With the aim to have one single calibration specimen, we engraved two gratings in the transversal and axial directions (Fig. 12), which allows us to do both calibrations.

Although the laser engraved lines have a nominal width of 25 μm with a 50 μm pitch, the real width has to be measured by a traceable calibrated instrument, which will yield the nominal value and the accumulated uncertainty.

The procedure to calibrate the rotating speed is very similar to the one depicted in Section 4.B.1, but with the acquisition of an unrolled image (Fig. 13). The obtained value PS_m has to be compared to the real PS_m of the specimen, and the factor is obtained by the division of the latter by the former applied to the rotating speed.

C. Parfocal and Parcentric Offsets, and Light Efficiency between Objectives

To obtain centered images with different objectives, parfocal and parcentric misalignments between them have to be adjusted. Additionally, every objective could have different light efficiency due to different numerical apertures. A light factor between them is calibrated to take this effect into account.

1. Parfocal and Parcentric Offset Calibration

Because of the microscope objective and nosepiece fabrication tolerances, the focal plane of an objective could be different from another objective, resulting in a parfocal error. Same would happen with optical axis deviation, which would make

the image appear displaced laterally between two objectives. These two errors can be compensated for with an automatic XYZ adjustment. In our case, we have defined a reference objective (5× magnification) to calibrate the rest. The procedure is manual: the user has to focus a small feature on a sample and center it in a certain region of the image. After changing the objective, the user has to repeat the same process by actuating the XYZ controls. The offsets between the actual and former positions correspond to the parfocal and parcentric adjustment of the latter objective.

2. Light Factor Calibration

Objectives can have different light efficiencies. To avoid adjusting light intensity in every objective change, we have assigned a light factor to each one. To adjust them, we start from a reference objective that has this factor set to 1. The process is automatic: a back light autolight is performed, the objective to calibrate is positioned, and light is adjusted iteratively until the gray level in the central region of the image is the same as that of the reference objective.

Although this light factor works satisfactorily with the back light, behavior is different with the epi-illumination, since this light crosses the objective twice. We calibrate separately an epi-light factor by focusing a sample.

D. Aliasing in High-Speed Image Acquisition

Aliasing may appear due to the coupling of frame rate and illumination pulse width modulation (PWM) switching frequency, which in our case is 15 kHz and 12 bits (4096 levels). Frame integration time has to be adjusted to minimize this effect. As can be seen in Fig. 14(a), a desynchronization between lighting and acquisition can lead to uneven light intensity across the image, whereas a well-adjusted acquisition time makes this effect unnoticeable [Fig. 14(b)].

5. ERROR SOURCES

To accomplish the required image quality, the roller stage components require strict manufacturing tolerances. Small deviations of these parts are translated into focus errors, wrong magnification images, or even wrong positioning of the stent under the microscope. We have detected two types of error that impose critical manufacturing tolerances: axis skewness and roller excentricity.

A. Axis Skewness

When assembling the roller stage, the center-to-center line between the two rollers has to be perpendicular to the optical axis and to the Z translation stage. If a skewness error is present between these two axes, different stents of different diameters will not focus onto its apex, but at a slightly lateral shift. To minimize this effect, we have established that the maximum angular error is the one that shifts the apex between the smallest and largest stent diameters that the system can measure by 3 pixels of a 5 × objective. In Fig. 15, a zoom view of a roller stage section with a stent of 1.5 mm outer diameter is shown.

To determine the Y and Z positioning errors (ΔY and ΔZ), first of all we determine the stent apex Z position (Z') with respect to the roller center:

$$Z' = \frac{D}{2} + \sqrt{\left(\frac{D_R}{2} + \frac{D}{2}\right)^2 - \frac{S^2}{4}}. \tag{8}$$

Here, $D/2$ corresponds to the stent outer diameter, D_R to the roller diameter, and S to the distance between the two rollers axes. Then, the distance M between the plane formed by the roller axes and the stent surface along the Z skew axis is calculated through

$$M = \left(Z' - \frac{D}{2}\right)\cos\gamma + \sqrt{\left(\left(Z' - \frac{D}{2}\right)\cos\gamma\right)^2 + DZ' - Z'^2}. \tag{9}$$

Here, γ is the angle formed by the Z and the optical axes. Finally, we obtain the Y and Z positioning errors through

$$\Delta Y = M \sin\gamma, \tag{10}$$

$$\Delta Z = Z' - M\cos\gamma. \tag{11}$$

Figure 16 shows the displacement in the Y direction (ΔY) as a function of the skewness angle γ for three different stent outer diameters. A reference Y error limit has also been plotted, corresponding to 3 pixels error for a 5× lens.

As can be seen in the figure, maximum allowed skewness error is below 1 arcmin, which means an extremely tight manufacturing tolerance. To reduce such tolerance, we have characterized this error by measuring the apex Y position of three different glass rods with diameters of 2, 5, and 10 mm. This characterization opens the possibility to shift the Y stage when loading a new stent into its correct position.

As regards the error in the Z direction, Fig. 17 shows that the error remains below 12 μm for skewness under 1.6 arcmin.

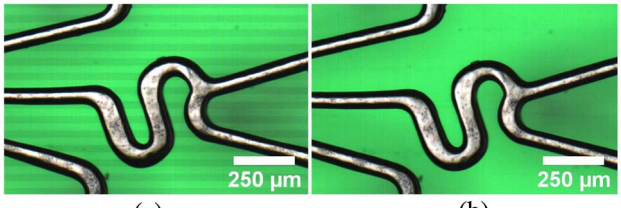

Fig. 14. Unrolled image taken at 997 fps; integration times of (a) 814 μs and (b) 849 μs.

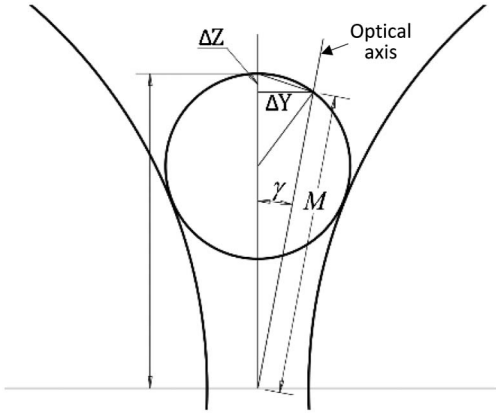

Fig. 15. Skewness error determination.

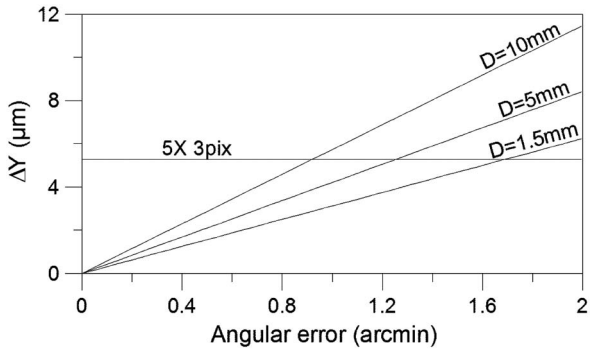

Fig. 16. Stent apex displacement in the Y direction as a function of skewness.

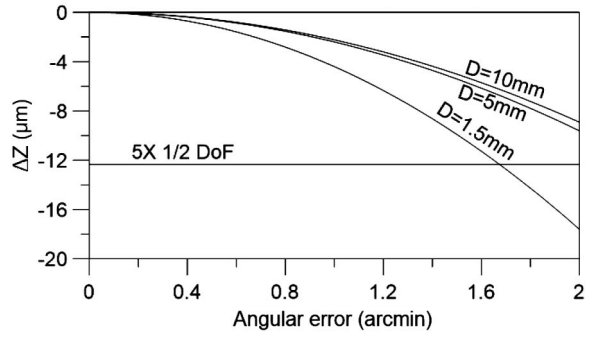

Fig. 17. Stent apex displacement in the Z direction as a function of skewness.

The maximum allowed error corresponding to the half of the DoF of a 5× 0.15 NA lens, that is 12.33 μm for a $\lambda = 555$ nm.

B. Roller Run-Out

Each roller could have form deviations from the nominal cylindrical shape, and its rotational axis to be not totally parallel. During roller revolution, these deviations mean that the rollers locally separate or approach each other, making the stent shift laterally and out of focus. We have established that the maximum excentricity error allowed is the one that keeps the stent within the DoF of the objective and a maximum of 3 pixels shift.

Figure 18 shows a zoom view of the roller stage with one eccentric roller.

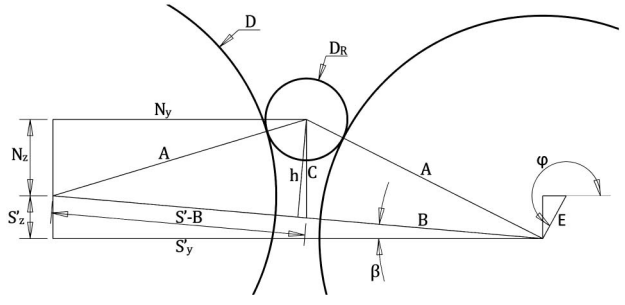

Fig. 18. Excentricity error determination.

Stent position is determined with N_y and N_z, which are referenced to the non-eccentric roller on the left. The excentricity effect is determined by the following equations:

$$S'_x = S + E\cos\varphi, \tag{12}$$

$$S'_y = E\sin\varphi, \tag{13}$$

$$\beta = \tan\left(\frac{S'_y}{S'_z}\right), \tag{14}$$

$$S' = \sqrt{S'^2_y + S'^2_z}, \tag{15}$$

where E is the constant, construction-defined excentricity error, S the roller axes theoretical separation, S' the real separation, which changes with the rotation angle ϕ, and β the angle formed by the two roller axes and the horizontal plane. To reach the stent dynamic position, some intermediate variables (h, B, and C) have to be described:

$$A^2 = \left(\frac{S'^2}{2}\right) + h^2, \tag{16}$$

where A is the sum of the radii of the roller and the stent $(D_R/2 + D/2)$. B and C are obtained through

$$C = \sqrt{\frac{\left(A^2 - \frac{S'^2}{4}\right)}{1 - \cos^2\left(\frac{\pi}{2} - \beta\right)}}, \tag{17}$$

$$B = \frac{S}{2} + C\cos\left(\frac{\pi}{2} - \beta\right). \tag{18}$$

Finally, the stent position with respect to the stationary roller is determined by

$$N_Y = (S' - B)\cos\beta, \tag{19}$$

$$N_Z = C - (S' - B)\sin\beta. \tag{20}$$

Both functions represent sinusoidal curves with different amplitudes, phases, and offsets. Maximum errors are defined by these amplitudes or the peak-to-valley value. As regards the Y displacement, which has minima and maxima at rotation angle ϕ depending on the stent diameter, we have calculated numerically the angles where the maxima condition is met using the derivative and its displacement value:

$$PV_Y = N_{Y\,\mathrm{MAX}} - N_{Y\,\mathrm{MIN}}. \tag{21}$$

As a result, Fig. 19 shows the maximum Y error as a function of excentricity error, for three different stent diameters. The greater the stent diameter, the bigger the error due to the amplification effect of the stent apex distance to the stent–roller contact points.

The maximum allowed error corresponds to 3 pixels distance with the 5× lens. To meet this constraint, roller excentricity needs to be less than 5 μm in the case of a coronary stent of 1.5 mm.

As regards the error in the Z direction, we have determined numerically that the maxima is found at rotation angle $\varphi = \pi$ and the minima is at $\phi = 0$. Therefore, we define the maximum Z error as

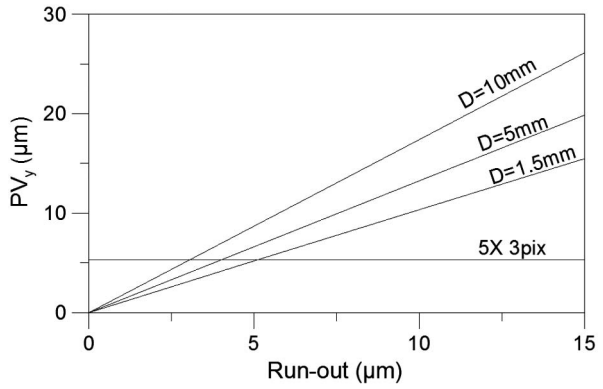

Fig. 19. Excentricity Y projection error for three different stents.

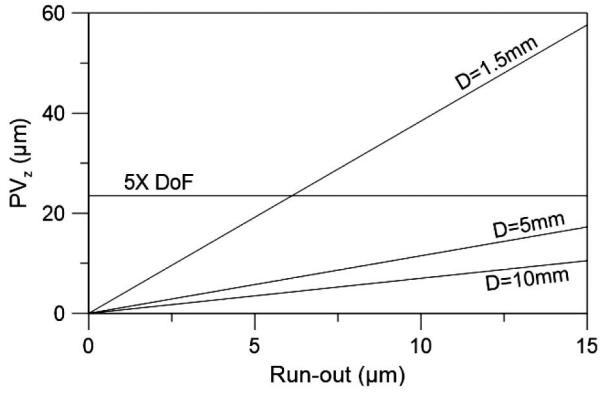

Fig. 20. Excentricity Z projection error for three different stents.

$$PV_Z = N_Z|_{\varphi=\pi} - N_Z|_{\varphi=0}. \quad (22)$$

In Fig. 20, the maximum Z error as a function of excentricity error is shown, for three different stent diameters. This error now decreases with the stent diameter because the roller contact point slope decreases.

As in Fig. 17, the maximum allowed limit is the DoF of the 5× lens as a reference. To keep the stent apex always in focus, the maximum allowed excentricity error is around 3 μm. This constraint is extremely tight for small diameters due not only to the vertical roller shift, but also the lateral roller contribution, which causes the stent to move vertically, as well.

The excentricity influence taking a stationary roller has been calculated. Taking into account that both rollers can have a specific excentricity, the maximum allowed error will be half of those stated above.

6. CONCLUSIONS

In this paper, a system for stent inspection is proposed. We have presented a novel lighting arrangement together with a high-precision rotational stage that allows us to acquire high-resolution images in a line-scan manner, which needed a specific, custom calibration specimen to evaluate its performance and calibrate its accuracy.

We have revealed that the critical dimension measurements with a conventional microscope differ from the real dimensions that can be obtained by our unrolled approach. We have also proposed the geometrical relationship between the two measurements.

As regards calibration, we have designed and manufactured a novel calibration specimen that allows us to calibrate the magnification of the system in the unrolled direction.

Finally, construction errors and tolerance limits have been identified to be able to perform said high-resolution images without defocus and to meet critical dimension measurement requirements.

REFERENCES

1. D. Freifeld, "Repetitive inspection system with intelligent tools," U.S. patent 6,606,403 (12 August 2003).
2. E. Maehringer-Kunz, M. Loeffler, R. Rode, T. Schneider, G. Jarschel, and K. Eggelbusch, "Automatic inspection device for stents, and method of automatic inspection," U.S. patent 20,090,251,535 A1 (30 August 2006).
3. I. Ibraheem and A. Binder, "An automated inspection system for stents," Int. J. Adv. Des. Manuf. Technol. **47**, 945–951 (2010).
4. F. Laguarta, C. Bermudez, R. Artigas, and C. Cadevall, "Device and method for optically inspecting and analysing stent-like objects," WO patent WO2015/096874 A1 (02 July 2015).